Conformal BiVO$_4$/WO$_3$ nanobowl array photoanode for efficient photoelectrochemical water splitting

Wen Zhang[a], Meng Tian[a], Haimiao Jiao[b], Hai-Ying Jiang*[a] and Junwang Tang*[b]

[a] *Key Laboratory of Synthetic and Natural Functional Molecule of the Ministry of Education, The Energy and Catalysis Hub, College of Chemistry and Materials Science, Northwest University, Xi'an 710127, P. R. China.*

[b] *Department of Chemical Engineering, University College London, Torrington Place, London WC1E 7JE, U.K.*

* Corresponding author

E-mail: jianghy@nwu.edu.cn (H. Jiang)

E-mail: junwang.tang@ucl.ac.uk (J. Tang)

ABSTRACT

As the most promising photoanode candidate for photoelectrochemical (PEC) water splitting, the photocurrent density of $BiVO_4$ still needs to be further improved in order to meet the practical application. In this work, a highly-matched $BiVO_4/WO_3$ nanobowl (NB) photoanode was constructed to enhance charge separation at the interface of the junction. Upon further modification of the $BiVO_4/WO_3NB$ surface by NiOOH/FeOOH as an oxygen evolution cocatalyst (OEC) layer, a high photocurrent density of 3.05 mA cm^{-2} at 1.23 V vs RHE has been achieved, which is about 5-fold higher than pristine $BiVO_4$ in neutral medium under AM 1.5 G illumination. 5 times higher IPCE at 450 nm is also achieved compared with $BiVO_4$ photoanode, leading to about 95% faradaic efficiency for both H_2 and O_2 gas production. Systematic studies attribute the significantly enhanced PEC performance to the smaller $BiVO_4$ particle size (< 90 nm) than its hole diffusion length (~100 nm), the improved charge separation of $BiVO_4$ by the single layer WO_3 nanobowl array and the function of OEC layers. Such WO_3NB possesses much smaller interface resistance with the substrate FTO glass and larger contact area with $BiVO_4$ nanoparticles. This approach provides new insights to design and fabricate $BiVO_4$-based heterojunction photoanode for higher PEC water splitting performance.

Keywords: PEC water splitting; WO_3 nanobowl; $BiVO_4$; Charge separation; NiOOH/FeOOH

1. Introduction

Photoelectrochemical (PEC) water splitting is a promising green technique for renewable hydrogen production [1-3]. To construct a practical PEC system, it is of great significance to develop efficient photoanodes. Bismuth vanadate (BiVO$_4$) has been identified as the most promising photoanode material because of its narrow band gap (ca. 2.4-2.5 eV) and favorable band positions for hydrogen and oxygen evolution [4-7]. Nevertheless, BiVO$_4$ has limitations of low carrier mobility (4×10^{-2} cm^2 V^{-1} s^{-1}) and short hole diffusion length (<100 nm) as a photoanode, resulting in unsatisfactory photocurrent densities [8,9] (<1 mA cm^{-2} at 1.23 V vs RHE in neutral medium under AM 1.5 G illumination). Except decreasing particle size of BiVO$_4$ to enable the hole transfer to its surface and depositing OEC layer to enhance the water oxidation kinetics, further effectively improving the charge separation efficiency of BiVO$_4$ is also worthy to be noted [10,11]. Therefore, inserting a new layer between BiVO$_4$ and FTO to resist this deficiency has been proposed and studied [12,13].

Among various semiconductor partners, BiVO$_4$/WO$_3$ is a proved type II heterojunction because of their favorable band alignment [14-17]. Importantly, previous studies found that the morphology of bottom WO$_3$ layer and the interfacial structure of BiVO$_4$/WO$_3$ play the important roles for the PEC process [18,19]. It has stimulated the majority of researches on the relationships between porosity control of the bottom layer and PEC efficiency. So far, various WO$_3$ with different morphologies, such as 1D nanowires/nanorods [19,20], 2D nanoplates/nanoflakes [15,21,22] and 3D inverse opal structures [23,24], have been demonstrated to be useful for enhancing the PEC performance of BiVO$_4$. The corresponding photocurrent density has been doubled, even tripled at 1.23 V vs RHE either in neutral medium or alkaline condition under AM 1.5 G illumination (Table S1). Furthermore, loading oxygen evolution cocatalysts (OECs), such as FeOOH [25,26], NiOOH/FeOOH [27, 28] or CoOOH [29] cocatalyst on the surface of BiVO$_4$ photoanode has been reported for further improving O$_2$ evolution kinetics and PEC performance. Despite these achieved significant progresses, the photocurrent and photo-electro conversion efficiency of BiVO$_4$ electrode are still

far from the application level. As reported, most of the previous WO_3 array on FTO electrode exhibited small array gaps (<60 nm), which is disadvantage for the uniform loading of $BiVO_4$ nanoparticles with the size of >80 nm. Also, some heterojunctions were fabricated in the form of simple bilayers, in which the upper layer of $BiVO_4$ was coated on the bottom WO_3 layer, exhibiting smaller contact area and unavoidable charge recombination in the bulk and boundary of $BiVO_4$ particles, thus leading to the unsatisfactory PEC process of $BiVO_4$. Therefore, conformally depositing the uniform $BiVO_4$ on the well-designed and highly-matched WO_3 bottom layer is still a great challenge. Based on monolayer colloidal crystals (MCC) method [30,31] with a low cost and high controllability for patterned nanostructures synthesis, nanobowl array fabrication is considered to be one of the best choices to construct the bottom layer for highly-matched $BiVO_4/WO_3$ heterojunctions.

Herein, WO_3 nanobowl (WO_3NB) array was synthesized by MCC process and for the first time used for constructing the highly-matched conformal $BiVO_4/WO_3NB/FTO$ heterojunction, which was utilized as a new type of photoanode to improve the PEC performance of $BiVO_4$. In this novel design, the small size of $BiVO_4$ nanoparticles (< 90 nm) was perfectly deposited on the bottom layer of WO_3 nanobowl with the large inner diameter of 920 nm. The smaller size of $BiVO_4$ than its hole diffusion length (~100 nm) ensures the holes transfer to its surface effectively, and then participating in the oxidation of water. Meanwhile, the highly ordered single-layer WO_3NB array was chosen to minimize the defects of WO_3 at the grain boundary, decrease the interfacial resistance with FTO and increase the contact area with $BiVO_4$ nanoparticles. Moreover, the highly-matched $BiVO_4/WO_3$ interface could also enhance the charge separation of $BiVO_4$, which plays the important role for the PEC process. With further loading an OEC layer on $BiVO_4/WO_3NB$ heterojunction photoanode, the produced photocurrent and IPCE exhibit about 5-fold higher than that over pristine $BiVO_4$ under one sun condition. The underlying reason of this enhanced PEC performance was then discussed.

2. Experimental section

2.1. Preparations

2.1.1. Preparation of WO₃NB photoanode

WO₃ nanobowl (WO₃NB) array was prepared using nanosphere lithography based on MCC method [30]. Briefly, MCC template with diameters of ~1 μm was assembled on the flurine-doped tin oxide (FTO) substrate, forming a colorful film (see Supplementary information). Then, the obtained electrode was immersed in the ammonium tungsten/methanol solution with the volume ratio of 2:1 for 30 minutes and dried at room temperature [32], guaranteeing that WO₃ precursor was infiltrated into the voids of the MCC template. The film was then heated at 475 °C for 2 hours in air with a heating rate of 1 °C min⁻¹. After the calcination process, MCC template was removed and WO₃ precursor in the void areas was converted into crystalline WO₃, forming WO₃NB array modified FTO substrate, while the corresponding photograph turned to translucent light yellow (Scheme 1). To investigate the effects of the thickness and morphology of WO₃ on the PEC performance of the BiVO₄/WO₃ photoanode, different concentrations (0.28, 0.14 and 0.07 g mL⁻¹) of ammonium tungsten/methanol solutions were adopted. The obtained WO₃ photoanodes were denoted as WO₃-1, WO₃-2, and WO₃NB, correspondingly.

2.1.2. Preparation of BiVO₄/WO₃NB photoanode

In order to construct a uniform BiVO₄/WO₃NB array, nanoparticle BiVO₄ with small size (~80) was *in-situ* grown on the inner surface of WO₃NB by a two-step electro-deposition method. Different to the previous report of direct BiOI deposition [10], Bi metal was firstly deposited on the inner face of WO₃NB in a three-electrode quartz cell system [13]. This process can increase the nucleation density of BiOI, and further promote the uniform coating of BiOI on the inner face of WO₃NB. Briefly, the electrolyte was prepared by dissolving Bi(NO₃)₃·5H₂O (0.1213 g) into an ethylene glycol/H₂O solution (37.5 ml) with the volume ratio of 2:1. The deposition process was carried out by giving the current of 4.34 ×10⁻² C cm⁻² at -0.6 V vs. Ag/AgCl. After this, Bi metal was successfully coated on the inner face of WO₃NB (Scheme 1). Being

washed with ethanol and dried at room temperature, the resulting electrodes were denoted as Bi@WO$_3$NB.

Then, Bi@WO$_3$NB was converted into BiVO$_4$/WO$_3$NB by electrochemical deposition of BiOI and annealing processes: Firstly, BiOI was deposited on the surface of Bi@WO$_3$NB in a three-electrode quartz cell system. The electrolyte was prepared by dissolving 0.907g Bi(NO$_3$)$_3$ 5H$_2$O and 3.32g KI in 50 mL H$_2$O , with adjusting the pH value to 1.7 by HNO$_3$ (6 M). Then, 20 mL ethanol containing 0.4987g *p*-benzoquinone was added into the solution above, and the obtained mixture was vigorously stirred for 15 min. Cathodic deposition was performed at -0.1 V vs. Ag/AgCl. In this regard, to achieve the maximum immobilization of BiVO$_4$ nanoparticle, the different electrodeposited times (0.5, 3, 4.5 and 6 min) of BiOI were carried out. The resulting electrodes were denoted as BiOI-*x*/Bi@WO$_3$NB (*x*=1-4). Subsequently, 0.15 mL dimethylsulfoxide solution containing 0.15 M VO(acac)$_2$ was placed on the BiOI-*x*/Bi@WO$_3$NB electrode, and was heated at 450 °C for 2 hours with a rate of 2 °C min^{-1} in air, to convert BiOI/Bi to BiVO$_4$. Excess V$_2$O$_5$ in the BiVO$_4$ photoanode was removed by soaking them in 1 M NaOH solution for 30 minutes with gentle stirring. The resultant photoanodes of BiVO$_4$-*x*/WO$_3$NB were rinsed with deionized water and dried in air. After these processes, the photoanode turned bright yellow (Scheme 1). In addition, the pure BiVO$_4$, BiVO$_4$/WO$_3$NL, BiVO$_4$/WO$_3$-1 and BiVO$_4$/WO$_3$-2 photoanode were obtained by the same experimental conditions when using FTO, WO$_3$NL, WO$_3$-1 or WO$_3$-2 as the substrates. The more detailed preparation procedures are described in the Supplementary material.

2.1.3. Preparation of OEC/BiVO$_4$/WO$_3$NB photoanode

A thin amorphous NiOOH/FeOOH layer, acting as an OEC layer, was introduced on the surface of BiVO$_4$/WO$_3$NB photoanode by a photo-assisted electrodeposition method [10] (Details for the sample fabrication can be referred to Experimental section in Supporting Information).

The whole fabrication process of OEC/BiVO$_4$/WO$_3$NB photoanode is illustrated in Scheme 1.
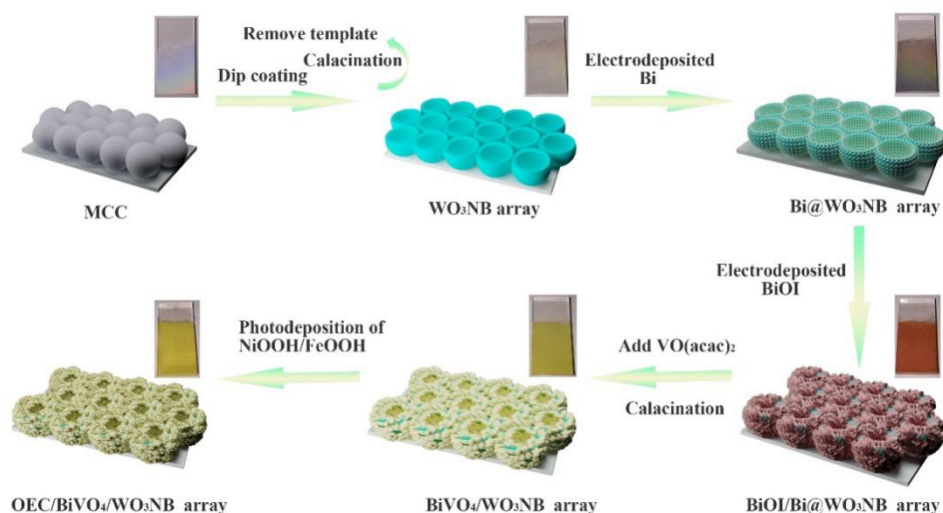
Scheme 1. Schematic illustration of the fabrication procedure of OEC/BiVO$_4$/WO$_3$NB array and corresponding photographic images of different photoanodes.

2.2.Characterization

The crystal structures were investigated by X-ray diffraction (XRD) patterns (Bruker AXS-D8 diffractometer) using Cu Kα radiation (λ = 0.154 18 nm) within the 2θ range from 10° to 80° at a scanning rate of 0.1° s^{-1}. Raman spectra were obtained from Renishaw Ramascope (confocal Raman microscope, Renishaw, Gloucestershire, U.K.) with a He−Ne laser (λ = 532 nm). The elemental compositions were measured by X-ray photoelectron spectroscopy (XPS, PHI5000 VersaProbeIII). All the data obtained from XPS spectra was calibrated by using the C 1s peak at the position of 284.8 eV. The morphologies of the samples were characterized by scanning electron microscopy (SEM, Hitachi SU8010) and (HR-TEM, FEI Tecnai G2 S-Twin F20). UV−vis diffuse reflectance spectra were executed on UV−vis spectrometer (UV-3600Plus, Shimadzu) equipped with integrated sphere method, and the Tauc plot curves were obtained from UV-vis DRS spectra to evaluate the band gaps of both the prepared WO$_3$NB and nanoporous BiVO$_4$. PL spectra were performed on fluorescence spectrophotometer (F-7100, Hitachi) with an excitation wavelength of 360 nm.

2.3.PEC measurements

PEC performances of the samples were carried out by employing a CHI660E electrochemical workstation with a typical three-electrode system. The simulated solar illumination was obtained by the light from a Xe 300 W lamp through an AM 1.5 G

filter with the light intensity of 100 mW cm^{-2}, which was measured by a thermopile optical detector (Newport, Model 818P-040-25). Samples were illuminated from the back side (FTO substrate side), with the illuminated area of 1.2 cm^2. Herein, 0.2 M Na$_2$SO$_4$ solution (pH=7) was used as the electrolyte for all PEC measurements. Electrochemical impedance spectroscopy (EIS) was also recorded with an AC voltage amplitude of 10 mV at the open circuit potentials of the films under AM 1.5 G illumination (frequency range of 0.01 Hz to 100 kHz). Photocurrent-potential curves were obtained using linear sweep voltammogram (LSV) in a voltage window of -0.4 V~1.1 V vs. Ag/AgCl with a scan rate of 10 mV s^{-1}. Incident-photon-to-current conversion efficiency (IPCE) was obtained using an Oriel Cornerstone 260 1/4 m monochromator coupled with a 300 W Xe arc lamp passed through an AM 1.5G filter as the simulated light source, and measured at 1.23 V vs. RHE in 0.2 M Na$_2$SO$_4$ solution. All the potentials vs. RHE were converted from the potentials vs. Ag/AgCl according to the Nernst equation: $E_{RHE}= E_{Ag/AgCl}+0.059$ pH$+0.197$. The as-obtained photoanodes, Ag/AgCl and Pt foil were used as the working, reference and counter electrodes, respectively.

2.4. Photoelectrochemical H$_2$ and O$_2$ evolution

Faradaic efficiency and photoelectrochemical H$_2$ and O$_2$ evolution were carried out in a two-electrode system, being composed of OEC/BiVO$_4$/WO$_3$NB as the photoanode and Pt as the counter electrode, in an airtight single cell with a bias of 0.9 V in 0.2 M Na$_2$SO$_4$ solution (pH 7). H$_2$ and O$_2$ evolution were analyzed by a gas chromatograph (SP-3420A, Beifen-Ruili).

3. Results and discussion
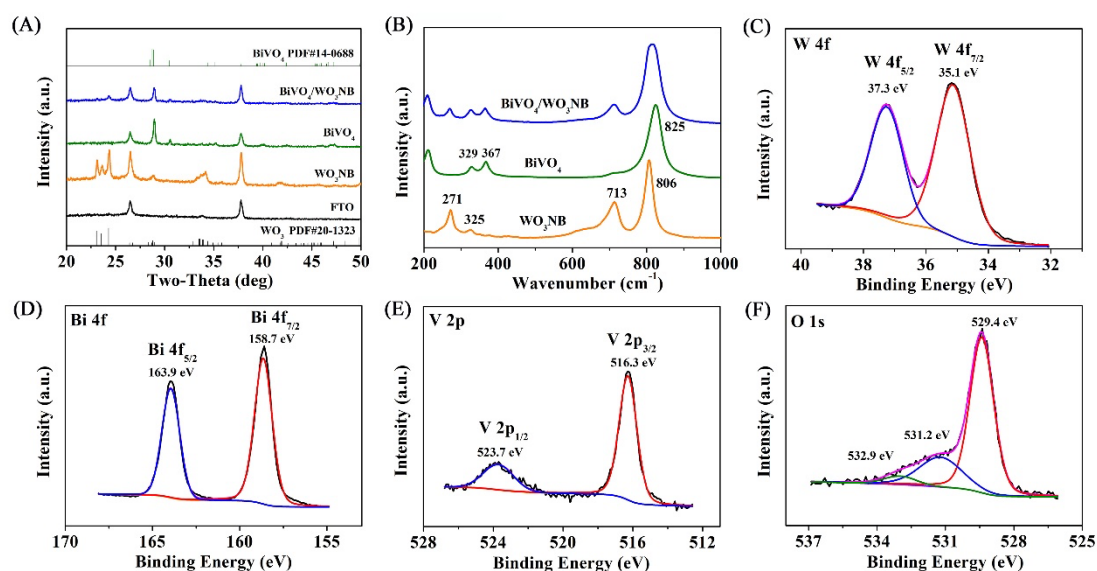
3.1. Materials characterization

Fig. 1. (A) XRD patterns of WO₃NB, BiVO₄ and BiVO₄/WO₃NB photoanodes. (B) Raman spectra of WO₃NB, BiVO₄, and BiVO₄/WO₃NB photoanodes excited under 532 nm laser. XPS core elemental spectra of BiVO₄/WO₃NB: C) W 4f, D) Bi 4f, E) V 2p, F) O 1s.

The crystalline phase structures of the prepared WO₃NB, BiVO₄ and BiVO₄/WO₃NB photoanodes were all characterized by X-ray diffraction (XRD) patterns, as shown in Fig. 1A. For WO₃NB, the main diffraction peaks with 2θ values of 23.1°, 23.6° and 24.3° match well with the (002), (020) and (200) crystal planes of monoclinic phase WO₃ (JCPDS No. 20-1323). For BiVO₄, the peaks at 28.9°, 30.5° and 35.2° could be indexed as the (121), (040) and (002) crystal planes, revealing the monoclinic phase BiVO₄ (JCPDS No. 14-0688). As expected, when BiOI@Bi/WO₃NB array was converted to BiVO₄/WO₃NB array by a chemical-thermal process, both the main diffraction peaks of WO₃NB and BiVO₄ appear in the XRD spectrum of BiVO₄/WO₃NB photoanode. Moreover, we note the (200) and (002) peaks of pristine BiVO₄ at $2\theta = 34.51°$ and 35.21°, as well as the (240) and (024) peaks of undistorted BiVO₄ at $2\theta = 46.7°$ and 47.3°, both converge to single peaks in the XRD spectra of BiVO₄/WO₃-1, BiVO₄/WO₃-2 and BiVO₄/WO₃NB (Fig. S1). The merging of peaks is attributed to a deformation of the scheelite crystal structure from monoclinic to tetragonal symmetry, in agreement with the previous reports [20, 33]. It is worth noting

that only partial merging of the peaks occurred on $BiVO_4/WO_3NB$, which is attributed to the relatively low amount of W doping and ultrathin thickness of bottom layer WO_3NB. XRD results confirm that W-doped $BiVO_4$ is formed at the interface of $BiVO_4/WO_3$ heterojunction. Thus, the as-prepared $BiVO_4/WO_3NB$ shows the intimate contact at the interface between $BiVO_4$ and WO_3NB, which can effectively enhance the charge transfer and prevent the recombination of photoelectrons and holes [12, 20].

Raman spectra were also conducted to further identify the crystal structures of WO_3NB, $BiVO_4$ and $BiVO_4/WO_3NB$. As can be seen in Fig. 1B, the as-obtained WO_3NB reveals four Raman peaks locating at 270, 330, 715 and 806 cm^{-1}, which can be attributed to the typical monoclinic WO_3 structure [34]. The peaks observed at 713 and 806 cm^{-1} belong to W-O stretching modes, and the peaks at 271 and 325 cm^{-1} can be assigned to the W-O-W bending vibrations of monoclinic phase WO_3 [15, 35]. The peaks of $BiVO_4$ at 329 and 367 cm^{-1} are ascribed to the asymmetric and symmetric bending vibration of the VO_4^{3-}, while the strong peak at 825 cm^{-1} is attributed to the symmetric V-O stretching mode in $BiVO_4$ [10]. After *in-situ* growth of $BiVO_4$ nanoparticles on WO_3NB array to obtain $BiVO_4/WO_3NB$ heterojunction, the Raman peaks derived from both WO_3NB and $BiVO_4$ are all observed, which are at 367, 271 and 713 cm^{-1}. Further, compared with $BiVO_4$ and WO_3NB, the peaks at 325 and 329 cm^{-1}, as well as the peaks at 806 and 825 cm^{-1}, both converge to form single peaks, again confirming the successful construction of $BiVO_4/WO_3NB$ heterostructure.

The elemental compositions and states of $BiVO_4/WO_3NB$ were measured by XPS. The full survey spectrum in Fig. S2 shows that the two-phase structure is mainly composed of W, Bi, V and O elements. From the high-resolution W4f XPS spectrum in Fig. 1C, the binding peaks at 35.1 eV and 37.3 eV are in accordance with W $4f_{7/2}$ and W4$f_{5/2}$, respectively.[38] The peaks of the Bi $4f_{5/2}$ and $4f_{7/2}$ spectra at 158.7 eV and 163.9 eV (Fig. 1D) can be attributed to the surface Bi^{3+} species [38]. The peaks of V $2p_{3/2}$ and V $2p_{1/2}$ are at around 516.3 eV and 523.7 eV (Fig. 1E), which are typical values for V^{5+} in $BiVO_4$[15, 36]. Meanwhile, the asymmetric O 1s XPS signals are fitted by three peaks at 529.4, 531.2 and 532.9 eV (Fig. 1F), indicating the lattice oxygen of $BiVO_4$ crystallites, WO_3NB and adsorbed water species, correspondingly [38-40].

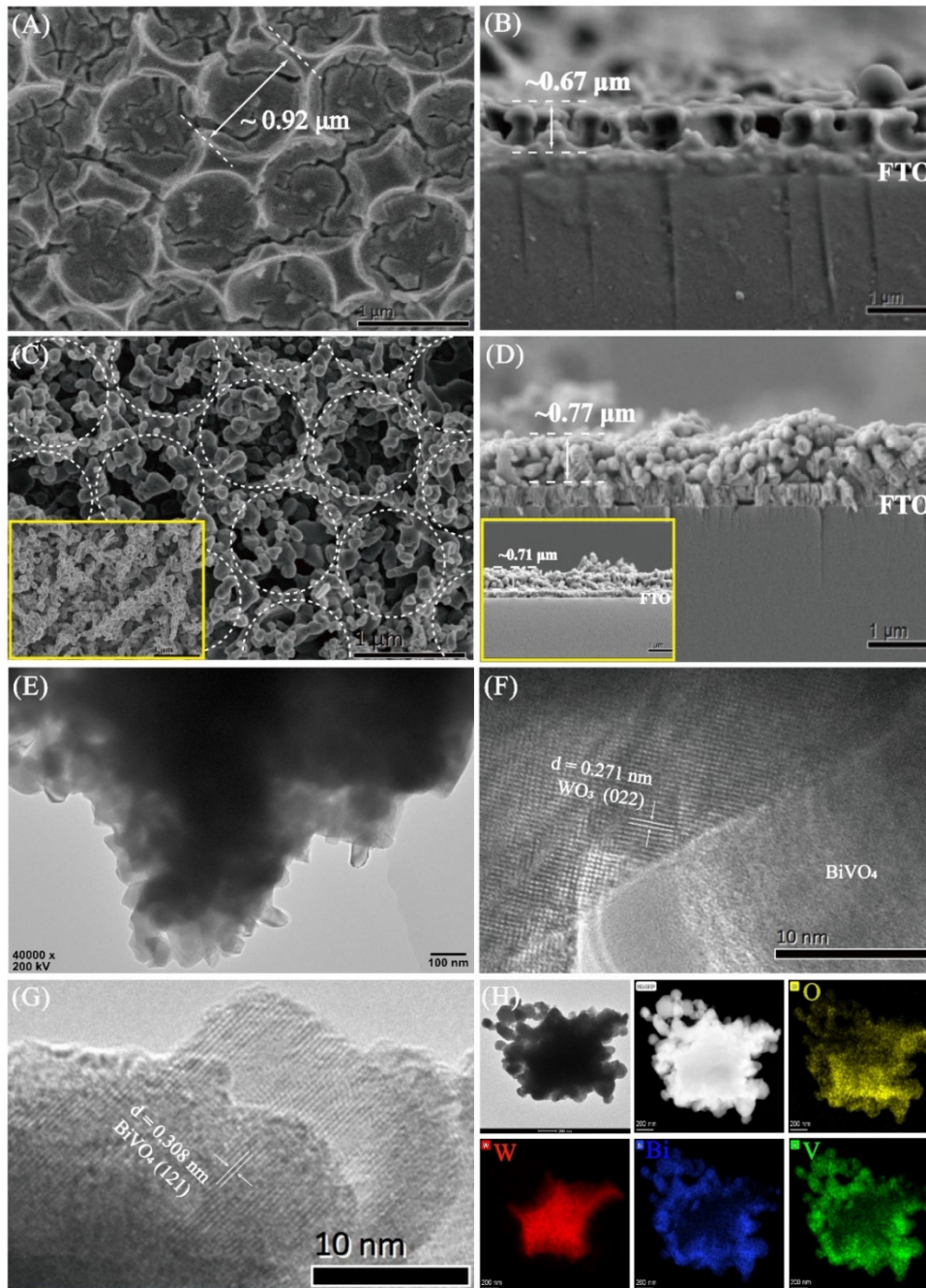## 3.2. SEM/TEM microstructure observations and EDX composition measurement

Fig. 2. Top-view and cross-sectional SEM images of WO$_3$ nanobowl photoanode (A, B) and BiVO$_4$/WO$_3$NB array (C, D). Insets in panels (C) and (D) are top-view and cross-sectional SEM image of pristine BiVO$_4$ photoanode, respectively. (E) TEM images and (F, G) HR-TEM images of BiVO$_4$/WO$_3$NB array. (H) TEM, HAADF and corresponding EDX elemental mapping images of O, W, Bi and V.

In order to prepare uniform single-layer WO$_3$NB array, different concentrations of WO$_3$ precursor solution were adopted, and the SEM images of WO$_3$-1, WO$_3$-2 and

WO$_3$NB photoanodes were observed. As shown in Fig. S3 and Fig. 2A-B, with the concentration of ammonium tungsten decreasing, the morphology of WO$_3$ nanobowl gradually appears. When the concentration of ammonium tungsten decreased from 0.28 g mL^{-1} to 0.14 g mL^{-1}, the thickness of the WO$_3$ decreases from 3.03 μm (WO$_3$-1, Fig. S3A and B) to 1.93 μm (WO$_3$-2, Fig. S3C and D). Further decreasing the concentration of ammonium tungsten to 0.07 g mL^{-1}, the single-layer WO$_3$NB array with 0.67 μm in thickness is produced, as depicted in Fig. 2B. Fig. 2A suggests that WO$_3$NB has a relatively rough bottom and about 920 nm diameters, which is in good agreement with the size of the polystyrene (1 μm). The enlarged SEM images in Fig. S4 clearly show the morphology of the obtained WO$_3$NB array, retaining the long-range hexagonal order stemmed from the initial MCC template. According to SEM images, it is clearly seen that we can easily control the concentration of WO$_3$ precursor solution to obtain the optimum morphology of single-layer WO$_3$NB array.

After in-situ growth of BiVO$_4$ nanoparticle on the WO$_3$NB array, both the bottom and wall of WO$_3$NB array (Fig. 2C, D) are uniformly covered with BiVO$_4$ nanoparticles. The mean particle size of BiVO$_4$ shown in Fig. 2C is 83±5 nm (Fig. S5). Meanwhile, the periodic structures of ordered WO$_3$NB are well maintained, as marked in white dotted circle in Fig. 2C. Inserts in Fig. 2C and D show the top-view and cross-sectional SEM of pristine BiVO$_4$ on FTO substrate, respectively. As also seen from Fig. 2D, the thickness of BiVO$_4$/WO$_3$NB array is obviously increased to 0.77 μm by comparing with that of pristine BiVO$_4$ (0.71 μm), further confirming the fully filling of BiVO$_4$ nanoparticles in WO$_3$NB. More importantly, from Fig. 2C and D, as well as their insets, it is clearly seen that the size and morphology of BiVO$_4$ are well maintained without disrupting.

Furthermore, the BiVO$_4$/WO$_3$-1 and BiVO$_4$/WO$_3$-2 photoanodes were also obtained and explored by SEM, as depicted in Fig. S6A-D. Similar to BiVO$_4$/WO$_3$NB array, the BiVO$_4$ is tightly attached and filled on the surface and in the gaps of WO$_3$-1 and WO$_3$-2 arrays, which further implies that highly uniform BiVO$_4$/WO$_3$NB array were successfully prepared in this work. Meanwhile, the images of the prepared WO$_3$NL and BiVO$_4$/WO$_3$NL photoanodes are also displayed in Fig. S6E-H for further

comparison.

To identify the morphology and distribution of $BiVO_4/WO_3NB$ heterojunction, high-resolution transmission electron microscopy (HR-TEM) and energy dispersive X-ray (EDX) elemental mapping were also employed. TEM image of $BiVO_4/WO_3NB$ is displayed in Fig. 2E. The crystalline structure of $BiVO_4/WO_3NB$ was further confirmed by HR-TEM image. In Fig. 2F, the measured lattice spacing of 0.271 nm is well matched with (022) crystal plane of monoclinic WO_3 in XRD pattern (Fig. 1A), while the lattice spacing of 0.308 nm (Fig. 2G) is in good agreement with (121) plane of monoclinic $BiVO_4$. TEM and HR-TRM images clearly indicate good formation of $BiVO_4/WO_3NB$ heterojunction, which is further confirmed by EDX with the coexistence of O, W, Bi and V elements, as well as the homogeneous distribution in the obtained $BiVO_4/WO_3NB$ heterojunction.

From Fig. 2H, it is also apparent that there is intimate contact at the interface between $BiVO_4$ and WO_3NB, which can efficiently enhance the charge transfer and prevent the recombination of photocarriers at the interface. In addition, Fe and Ni elements have been found to be evenly distributed on the photoanode of $OEC/BiVO_4/WO_3NB$ after deposition of NiOOH/FeOOH, according to the EDX elemental mapping in Fig. S7E-L. HR-TEM images (Fig. S7A-D) also exhibit a thin amorphous NiOOH/FeOOH layer, demonstrating the successful deposition of the OEC layer. The XPS spectra of $OEC/BiVO_4/WO_3NB$ were shown in Fig. S8. Fig. S8A shows the Fe 2p with two major peaks of ~ 711.4 eV (Fe $2p_{3/2}$) and ~725.1 eV (Fe $2p_{1/2}$), which are a good evidence to validate the presence of FeOOH [25]. The Ni 2p has a small Ni $2p_{3/2}$ peak at ~856.1 eV and an associated satellite peak at ~861.3 eV (Fig. S8B), revealing that the oxidation state of Ni is 2+ [41]. Meanwhile, the asymmetric O 1s XPS spectrum in Fig. S8C was fitted to two peaks at 530.1 and 531.6 eV, corresponding to O^{2-} and OH^-, respectively [42].

3.3. UV-vis analysis

The light absorbance ability is regarded as a key factor on light-to-energy conversion efficiency. Therefore, we investigated UV−vis absorption spectra of different photoanodes, as displayed in Fig. 3. It can be seen that the absorption edge of

WO₃NB and BiVO₄ photoanodes are located at the wavelength of ~450 nm and ~510 nm, respectively. For BiVO₄/WO₃NB photoanode, it shows nearly the same absorption edge as that of pure BiVO₄, with the absorption onset at ~510 nm and a smooth rise for most of the light adsorption in the entire 300-510 nm wavelength range. This result indicates that the light absorption of BiVO₄/WO₃NB photoanode mainly comes from the BiVO₄ rather than the under-layer WO₃NB. It should be noted that no obvious difference is observed between BiVO₄/WO₃NB and OEC/BiVO₄/WO₃NB, revealing that uniform and thin deposition of NiOOH/FeOOH would not affect the light absorption of BiVO₄/WO₃NB, which is consistent with our previous studies [37].
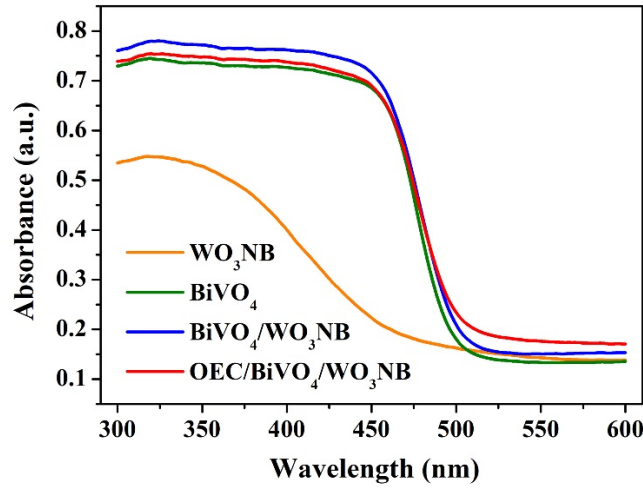

Fig. 3. UV−vis absorption plots of different photoanodes

To investigate the matching degree of the bands between WO₃NB and BiVO₄, the energy band structures of pristine WO₃NB and BiVO₄ were studied. The band gaps (E_g) of WO₃NB and BiVO₄ were calculated according to Tauc equation:

$$(\alpha h\upsilon)^n = A(h\upsilon - E_g)$$

Where α and $h\upsilon$ represent the absorbance coefficient and the energy of photon, respectively; n is the index which depends on the electronic transition of the semiconductor (for direct band-gap semiconductors BiVO₄ and WO₃, $n = 2$) [7, 38]; A is a proportionality constant related to the materials. On the basis of the results in Fig. 3, the band gap of WO₃ was determined to be 2.79 eV (Fig. S9A), while the band gap of BiVO₄ was determined to be 2.52 eV (Fig. S9B), which are consistent with the previous reports [10, 39]. The conducting behavior of the WO₃NB and BiVO₄

photoelectrodes were also analyzed by Mott-Schottky (M-S) experiments. Typically, M-S plots were measured at an applied frequency of 1000 Hz in 0.2 M Na_2SO_4 electrolyte under dark conditions. As shown in Fig. S9C and D, WO_3NB and $BiVO_4$ show the positive slopes, demonstrating that they are typical n-type semiconductors. Furthermore, the *x*-axis intercept of M–S plots can be used to determine the flat band potentials (E_{fb}) of photoelectrodes [12]. From the intercepts of the M–S plots, the E_{fb} of WO_3NB photoelectrode was estimated to be -0.12 V (vs Ag/AgCl) or 0.49 V (vs RHE) from Fig. S9C, while the E_{fb} for $BiVO_4$ nanoparticle was estimated as -0.57 V (vs Ag/AgCl) or 0.04 V (vs RHE) from Fig. S9D, as also shown in Table S2. It is widely accepted that the flat band potential (E_{fb}) is close to the bottom of the conduction band (CB) of n-type semiconductors [5]. On the basis of above analyses, the band level alignments of WO_3 with a band gap of 2.79 eV and $BiVO_4$ with a bandgap of 2.52 eV are thus presented in Fig. S10, indicating a type II band alignment. The observed more negative E_{fb} value of $BiVO_4$ compared with that of WO_3NB suggests feasible the injection of photogenerated electrons from $BiVO_4$ to WO_3. The flow of photogenerated holes from WO_3 to $BiVO_4$ can also thermodynamically occur, resulting into to the enhanced photocarriers separation at the interface between WO_3NB and $BiVO_4$ [38].

3.4. PEC Performances

PEC performance of the WO_3NB array was evaluated in 0.2 M Na_2SO_4 under AM 1.5 G simulated solar light (100 mW cm^{-2}). For comparison, PEC performances of the obtained WO_3-1 and WO_3-2 films were also measured under the same conditions. As seen from Fig. S11A, the photocurrent density is obviously associated with the thickness of WO_3 film, while WO_3NB photoanode shows the smallest photocurrent than WO_3-1 and WO_3-2. This is ascribed to the lowest light absorption ability of WO_3NB array due to its thinnest thickness. Encouragingly, the photocurrent densities of all investigated $BiVO_4/WO_3$ heterojunctions are increased dramatically (Fig. S11B) after in situ growth of $BiVO_4$ nanoparticles on different WO_3 films. It is worth to be note that the photocurrent densities of the prepared $BiVO_4/WO_3NB$ photoanodes show an increasing trend with the decreasing thickness of WO_3NB. These results reveal that

the microstructure of WO_3 will influence the interfacial charge transfer between $BiVO_4$ and WO_3NB, which plays the important role for the PEC activity of $BiVO_4/WO_3NB$ photoanode. To further confirm this conclusion, WO_3 nanolayer (WO_3NL) and $BiVO_4/WO_3NL$ were also prepared with the WO_3 thickness of 550 nm. Obviously, $BiVO_4/WO_3NB$ photoanode shows a higher photocurrent density than $BiVO_4/WO_3NL$ (Fig. S11D), although the latter shows a higher photocurrent density than the former when the onset potential is below 0.9 V vs RHE and above 1.5 V vs RHE (Fig. S11C).
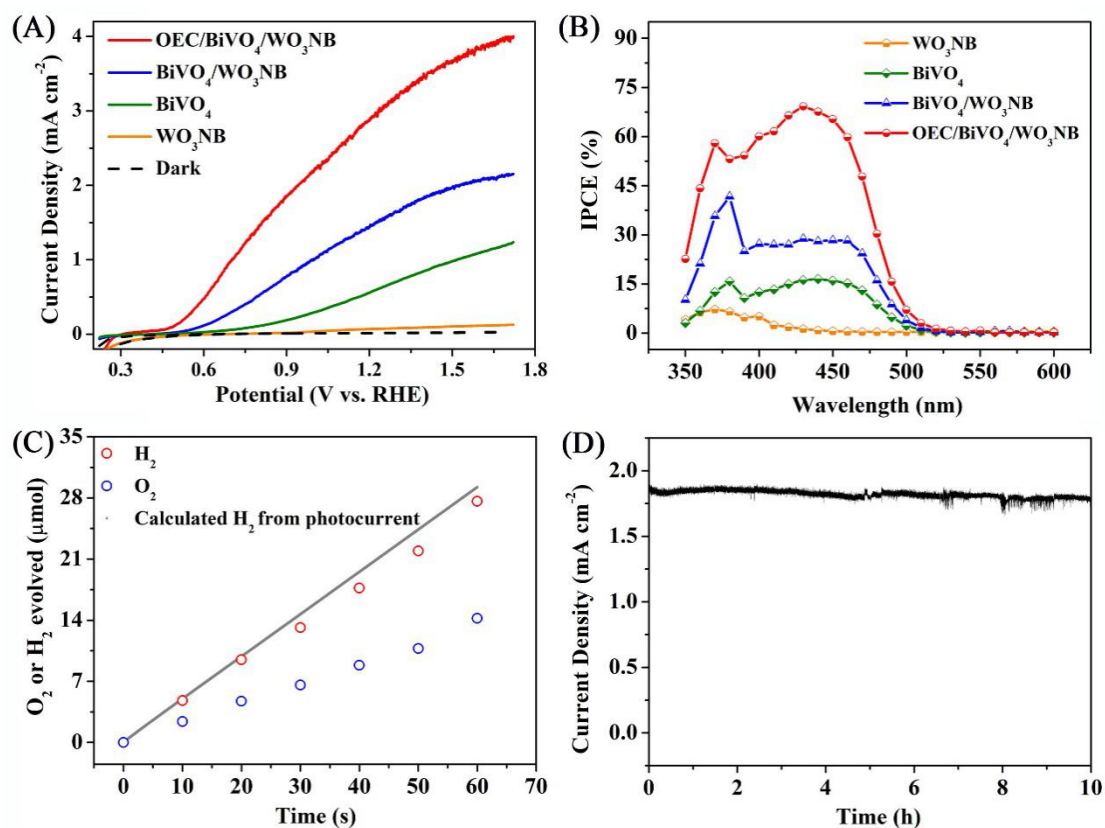

Fig. 4. (A) $J-V$ curves measured of WO_3NB, $BiVO_4$, $BiVO_4/WO_3NB$, and $OEC/BiVO_4/WO_3NB$ array for water oxidation (0.2 M Na_2SO_4) electrolyte, simulated solar light (AM 1.5 G 100 mW cm^{-2}) illumination. (B) IPCE of WO_3NB, $BiVO_4$, $BiVO_4/WO_3NB$ and $OEC/BiVO_4/WO_3NB$ photoanodes. IPCE was measured at 1.23 V vs RHE. (C) Detection of H_2 and O_2 produced by $OEC/BiVO_4/WO_3NB$ array at 0.9 V vs counter electrode. Gray dotted line represents the amount of H_2 calculated assuming 100% faradaic efficiency. (D) Stability testing of the $OEC/BiVO_4/WO_3NB$ array photoanode at 0.9 V (vs RHE) for 10 h. Electrolyte: 0.2 M Na_2SO_4 (pH =7).

Meanwhile, we also note that $BiVO_4/WO_3NB$ photoanode exhibits the significant improvement for the photocurrent density, compared with that on WO_3NB photoanode.

BiVO$_4$/WO$_3$NB photoanodes with different amount of BiVO$_4$ were also prepared to get the optimized photoanode with the highest photocurrent density. From the results in Fig. S12, the highest photocurrent (1.51 mA cm^{-2} at 1.23 V vs RHE) was achieved on BiVO$_4$-3/WO$_3$NB with the BiOI deposition time of 270 s, which is 2.5 times higher than that on BiVO$_4$ photoanode (0.61 mA cm^{-2} at 1.23 V vs RHE) and more than 20 times higher than that on WO$_3$NB photoanode (0.07 mA cm^{-2} at 1.23 V vs RHE), which are displayed in Fig. 4A.

For further improvement of water oxidation ability, NiOOH/FeOOH was deposited on the surface of the prepared BiVO$_4$/WO$_3$NB photoanode as an OEC layer. As expected, the as-fabricated OEC/BiVO$_4$/WO$_3$NB photoanode exhibits a markable improvement in photocurrent (3.05 mA cm^{-2} at 1.23 V vs RHE), which is twice higher than that on BiVO$_4$/WO$_3$NB photoanode. It is worthy to note that although the deposition of OEC layer does not change the light absorption of BiVO$_4$/WO$_3$NB photoanode (Fig. 3), it is able to create an adequate junction onto BiVO$_4$/WO$_3$NB, thereby further improving the kinetics of water oxidation [10, 43]. Accordingly, the OEC layer can efficiently facilitate the hole transfer from BiVO$_4$ to OEC layer and the water oxidation kinetics. On the other hand, the conduction band electrons of BiVO$_4$ effectively channeled to FTO and the counter electrode *via* the under-layer of WO$_3$NB. The two assisted junctions of OEC/BiVO$_4$ and BiVO$_4$/WO$_3$NB synergistically improved PEC performance of BiVO$_4$ photoanode. The photocurrent properties of water splitting behaviors on BiVO$_4$/WO$_3$ photoanodes in neutral medium are compared with previous studies in recent years (Table S1).

The incident photon to current conversion efficiencies (IPCE) were performed to study the wavelength dependent photoactivity efficiency of the prepared photoanode, and defined as follow:

$$IPCE(\%) = \frac{1240 \times J \,(\text{mA cm}^{-2})}{P_{\text{light}} \,(\text{mW cm}^{-2}) \times \lambda \,(\text{nm})} \times 100$$

Where J presents the photocurrent density, λ is the wavelength of incident light, and P_{light} is the incident light power density at a certain wavelength. In Fig. 4B, the WO$_3$NB shows the photocurrent response range of 350-430 nm, whereas BiVO$_4$ shows

a wider photocurrent response range of 350-510 nm, which are accordance with their UV-vis absorption spectra. Both WO_3NB and $BiVO_4$ photoanodes show comparatively low IPCE values, which are consistent with the previously reported films of similar photoanodes [10, 44]. Remarkably, the IPCE of $BiVO_4/WO_3NB$ photoanode is about 40% at 390 nm, almost 2.5 times higher than that of pristine $BiVO_4$ (16.2%). This result demonstrates that WO_3NB could effectively improve the charge separation of $BiVO_4$, further increasing the solar energy conversion efficiency. In contrast, the $OEC/BiVO_4/WO_3NB$ photoanode presents a much higher IPCE value than that of $BiVO_4/WO_3NB$, in agreement with previous report [29], in which the OEC layer could significantly improve the charge carrier separation rate of photoanode. In addition, since the WO_3NB first absorbs part of the photons with wavelengths < 400nm, reducing the UV photons to be absorbed by the top layer $BiVO_4$ in the UV region. Therefore, the IPCE value of $BiVO_4/WO_3NB$ and $OEC/BiVO_4/WO_3NB$ is higher in visible region than that in UV region. The IPCE results are in good accordance with the $J-V$ measurements as mentioned above. Furthermore, the applied bias photon to current efficiency (ABPE) values of all the photoanodes are shown in Fig. S13. The ABPE value of pure WO_3NB is negligible (0.01%), while only 0.04% at 0.9 V vs RHE for $BiVO_4$ is obtained. Significantly, the as-fabricated $BiVO_4/WO_3NB$ heterojunction can boost the ABPE to 0.25% at 0.9 V vs RHE. Specially, after depositing NiOOH/FeOOH layer, the obtained $OEC/BiVO_4/WO_3NB$ photoanode presents the maximum ABPE of 0.62% at 0.9 V vs RHE, which is 60, 15 and 2.5 times higher than those of WO_3NB, $BiVO_4$ and $BiVO_4/WO_3NB$ photoanodes, respectively.

PEC water splitting was carried out in 0.2 M Na_2SO_4 solution (pH = 7), by using a two-electrode system in an airtight single cell at the bias of 0.9 V vs counter electrode. As seen from Fig.4C, the amounts of produced H_2 and O_2 are linearly increased with the prolonging PEC reaction time, which are 27.6 μmol and 14.2 μmol after 60 minutes under consecutive light illumination and keep consistent with the stoichiometric ratio of 2:1. A faradaic efficiency as high as 95% is obtained, indicating that most of the photocurrent can be efficiently utilized to generate H_2 and O_2. In terms of practical application, the stability of $OEC/BiVO_4/WO_3NB$ photoelectrode was evaluated by a

long time run. The data in Fig. 4D indicates a good stability of the "triple" junction photoanode, with 96.7% photocurrent persistence after 10 hours' PEC reaction.
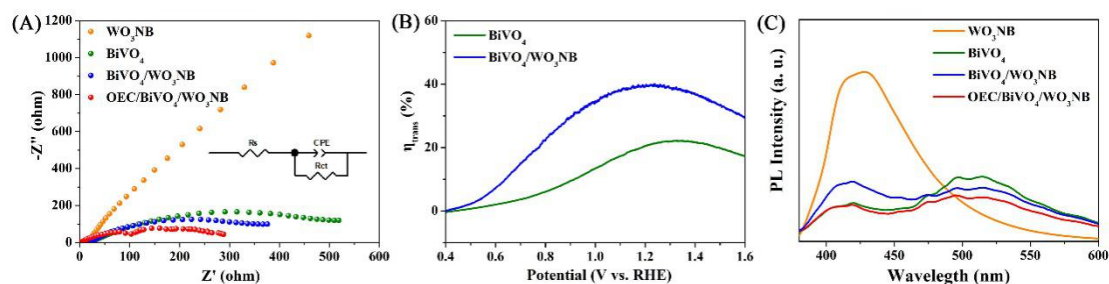

Fig. 5. (A) EIS curves of WO_3NB, $BiVO_4$, $BiVO_4/WO_3NB$ and $OEC/BiVO_4/WO_3NB$ array (B) Surface charge separation efficiency of $BiVO_4$ and $BiVO_4/WO_3NB$ photoanodes. (C) PL spectra of WO_3NB, $BiVO_4$, $BiVO_4/WO_3NB$ and $OEC/BiVO_4/WO_3NB$ photoanodes.

EIS curves of WO_3NB, $BiVO_4$, $BiVO_4/WO_3NB$ and $OEC/BiVO_4/WO_3NB$ photoanodes were carried out under AM 1.5G light illumination (Fig. 5A), in order to investigate the kinetics of charge transfer behavior during water splitting reaction. In the equivalent [29], R_s represents the system resistance, and R_{ct} reflects the charge transfer resistance. According to the fitting results (Table S3), a much smaller R_{ct} is observed for the $BiVO_4/WO_3NB$ photoanode compared with those of $BiVO_4$ and WO_3NB, implying the advantage of the heterostructure in the charge transfer process. These results prove that WO_3NB as an insert underlayer plays an important role on the electron transfer from $BiVO_4$ to FTO [19, 22]. After deposition of OEC layer on the surface of $BiVO_4/WO_3NB$ photoanode, the photoanode shows the lowest R_{ct} value (297.8 Ω), which could account for its highest PEC performance.

Since the oxidation of SO_3^{2-} by holes is very fast at the interface of photoanode/electrolyte, the surface recombination of charges is eliminated and η_{trans} (Na_2SO_3) ≈ 100%.[45] To further explore the interface recombination of $BiVO_4/WO_3NB$ photoanode, we measured the LSV curves of $BiVO_4$ and $BiVO_4/WO_3NB$ with and without Na_2SO_3. As shown in Fig. S14, the photocurrent for pristine $BiVO_4$ increases from 0.61 mA cm^{-2} to 2.71 mA cm^{-2} at 1.23 V vs RHE after the addition of Na_2SO_3. Notably, the photocurrent of $BiVO_4/WO_3NB$ is achieved at 3.67 mA cm^{-2} after the addition of Na_2SO_3 into electrolyte, which is higher than that of pure $BiVO_4$. These results confirm the efficient charge transfer from $BiVO_4$ to WO_3NB

in BiVO$_4$/WO$_3$NB photoanode, which can be attributed to the highly-matched BiVO$_4$/WO$_3$NB heterojunction [7, 43]. Furthermore, the surface transfer efficiencies (η_{trans}) can be individually determined by $J_{H_2O}/J_{Na_2SO_3}$. As evaluated, η_{trans} value of BiVO$_4$/WO$_3$NB is nearly 40%, much higher than that of pristine BiVO$_4$ (20%) in Fig. 5B, which could be attributed to the highly-matched conformal BiVO$_4$/WO$_3$NB heterojunction increasing electrolyte accessible area.

At last, photoluminescence (PL) spectra of WO$_3$NB, BiVO$_4$, BiVO$_4$/WO$_3$NB and OEC/BiVO$_4$/WO$_3$NB were performed to investigate their charge carrier separation rate. The results are shown in Fig. 5C. For pure WO$_3$NB and BiVO$_4$, the main emission peaks appear around 430 and 510 nm, near to their band-edge transitions of WO$_3$NB and BiVO$_4$, respectively. For BiVO$_4$/WO$_3$NB, both two major peaks around 430 and 510 nm are also observed. PL intensity of BiVO$_4$/WO$_3$NB are weaker than those of WO$_3$NB and BiVO$_4$, implying that the recombination of electron-hole pairs can be suppressed deeply by their junction structure. When BiVO$_4$/WO$_3$NB heterojunction is further combined with NiOOH/FeOOH, PL intensity is further decreased, suggesting the superior charge carrier separation rate of OEC/BiVO$_4$/WO$_3$NB photoanode.
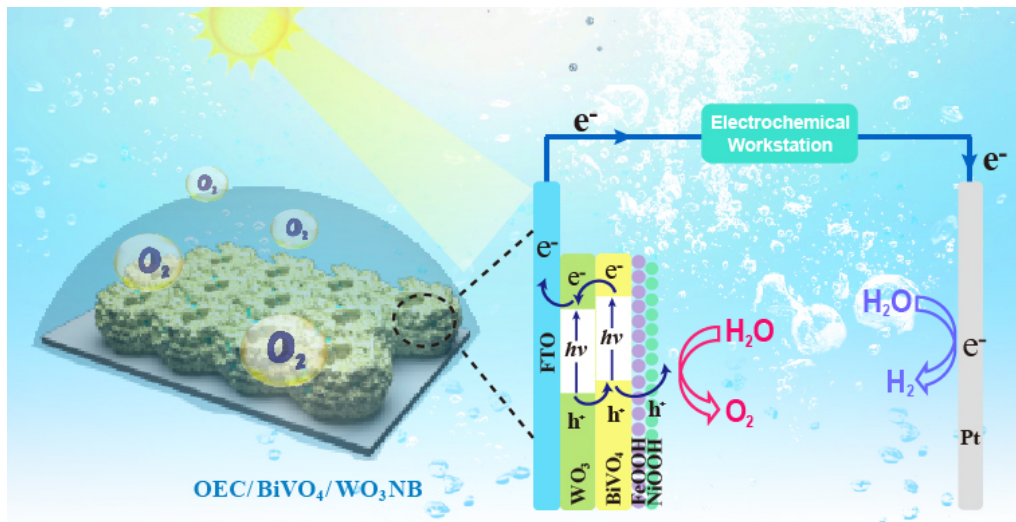
Scheme 2. The mechanism of charge carrier separation/transport and subsequent PEC reaction for the OEC/BiVO$_4$/WO$_3$NB photoanode.

On the basis of the results and discussions above, the mechanism on the high PEC water splitting activity over OEC/BiVO$_4$/WO$_3$NB photoanode is summarized in **Scheme 2**. The highly ordered WO$_3$NB arrays perfectly host the small size and nano-

structure of BiVO$_4$, which minimize the defects of WO$_3$ at the grain boundary, decrease the interfacial resistance with FTO and increase the contact area with BiVO$_4$ nanoparticles. Under light illumination, photogenerated electron−hole pairs are generated in both WO$_3$NB and BiVO$_4$ due to their favorable band gaps. With the formation of type II heterojunction, the excited electrons of BiVO$_4$ move to the conduction band of WO$_3$NB, then to FTO and the counter electrode of Pt for H$_2$ generation. Besides, WO$_3$NB plays a crucial role on the facilitation of electron transport from BiVO$_4$ to FTO, which can effectively reduce the photocarriers' recombination on the interface of BiVO$_4$/FTO junction. Meanwhile, the photogenerated holes in the valence band (VB) of WO$_3$NB will thermodynamically move to the valence band of BiVO$_4$, then transfer to NiOOH/FeOOH layer for O$_2$ evolution. Synergistically, the photogenerated carriers can be efficiently separated at the location. With the assistant of OEC, a high PEC performance of water oxidation over BiVO$_4$/WO$_3$NB heterojunction photoanode was achieved.

4. Conclusion

In summary, in order to improve the PEC performance of BiVO$_4$, we developed a facile and effective strategy to fabricate a highly-matched BiVO$_4$/WO$_3$ nanobowl array heterojunction, by conformal BiVO$_4$ nanoparticles (with the particle size of ~80 nm) in-situ grown on the single-layer of WO$_3$ nanobowl array. Upon modification by an OEC layer, the optimized BiVO$_4$/WO$_3$NB presents a maximum photocurrent density of 3.05 mA cm^{-2} at 1.23 V vs RHE in 0.2 M NaSO$_4$ electrolyte under AM 1.5 G illumination, resulting into stochiometric H$_2$ and O$_2$ production with a faradaic efficiency of 95%. Further analysis on the mechanism of such a high PEC performance attribute to the small BiVO$_4$ nanoparticles and single layer WO$_3$NB, as well as their highly matched electronic structure. The small BiVO$_4$ nanoparticles (< 90 nm) enable more holes to transfer to its surface; the single layer WO$_3$NB with large surface area and the highly matched BiVO$_4$/WO$_3$NB interface significantly enhanced the charge separation and transmission from BiVO$_4$ to WO$_3$NB, resulting into the charge separation efficiency increase by twice compared with BiVO$_4$. This thin layer of

WO$_3$NB further transfers electrons to FTO substrates due to the small interface resistance with FTO and large contact area with BiVO$_4$. With this "multiple" junctions as the photoanode, the photocarriers can successfully transmit in the electric circuit, participating the redox reactions on the corresponding electrodes. Overall, our work provides an efficient strategy to design and fabricate a "multiple" BiVO$_4$-based heterojunction with advantage architectures for efficient PEC water splitting.

Conflict of interest

The authors declare no conflict of interest.

References

[1]   C. Jiang, S. Moniz, A. Wang, T. Zhang, J. Tang, *Chem. Soc. Rev.,* **2017**, 46, 4645–4660.

[2]   Z. Li, W. Luo, M. Zhang, J. Feng, Z. Zou, *Energy Environ. Sci.,* **2013**, 6, 347–370.

[3]   Z. L. Wang, L. Z. Wang, *Chin. J. Catal.,* **2018**, 39, 369–378.

[4]   S. Ho-Kimura, S. Moniz, A. Handoko, J. Tang, *J. Mater. Chem. A,* **2014**, 2, 3948–3953.

[5]   Q. Z. Wang, T. J. Niu, L. Wang, J. W. Huang, H. She, *Chin. J. Catal.,* **2018**, 39, 613–618.

[6]   S. Wang, P. Chen, Y. Bai, J.-H. Yun, G. Liu, L. Wang, *Adv. Mater.,* **2018**, 30, 1800486–1800492.

[7]   S. Moniz, J. Zhu, J. Tang, *Adv. Energy Mater.*, **2014**, 4, 1301590–1301597.

[8]   S. Wang, T. He, P. Chen, A. Du, K. Ostrikov, W. Huang, L. Wang, *Adv. Mater.,* **2020**, 32, 2001385–2001394.

[9]   F. Abdi, T. Savenije, M. May, B. Dam, R. van de Krol, *J. Phys. Chem. Lett.,* **2013**, 4, 2752–2757.

[10]   T. Kim, K.-S. Choi, *Science,* **2014**, 343, 990–994.

[11]   D. Lee, K.-S. Choi, *Nat. Energy,* **2018**, 3, 53–60.

[12]   Q. Pan, H. Zhang, Y. Yang, C. Cheng, *Small*, **2019**, 15, 1900924–1900932.

[13]   J. Liu, J. Li, M. Shao, M. Wei, *J. Mater. Chem. A,* **2019**, 7, 6327–6336.

[14]   S. Khoomortezaei, H. Abdizadeh, M. Golobostanfard, *ACS Appl. Energy Mater.,* **2019**, 2, 6428–6439.

[15]   X. Zhang, X. Wang, D. Wang, J. Ye, *ACS Appl. Mater. Interfaces*, **2019**, 11, 5623–5631.

[16]   B. Chen, Z. Zhang, M. Baek, S. Kim, W. Kim, K. Yong, *Appl. Catal. B Environ.,* **2018**, 237, 763–771.

[17]   Y. Liu, B. Wygant, K. Kawashima, O. Mabayoje, T. Hong, S.-G. Lee, J. Lin, J.-H. Kim, K. Yubuta, W. Li, J. Li, C. Mullins, *Appl. Catal. B Environ.,* **2019**, 245, 227–239.

[18]   S. Chae, H. Jung, H. S. Jeon, B. K. Min, Y. Hwang, O.-S. Joo, *J. Mater. Chem. A,* **2014**, 2, 11408–11416.

[19]   M. Lee, D. Kim, W. Sohn, C. Moon, H. Park, S. Lee, H. Jang, *Nano Energy,* **2016**, 28, 250–260.

[20]   P. Rao, L. Cai, C. Liu, I. Cho, C. Lee, J. M. Weisse, P. Yang, X. Zheng, *Nano Lett.,* **2014**,

14, 1099–1105.

[21]   T. Zhang, J. Su, L. Guo, *CrystEngComm,* **2016**, 18, 8961–8970.

[22]   V. Kumbhar, H. Lee, J. Lee, K. Lee, *J. Colloid Interface Sci.,* **2019**, 557, 478–487.

[23]   K. Ouyang, S. Xie, P. Wang, J. Zhu, P. Zhan, *Int. J. Hydrogen Energy,* **2019**, 44, 7288–7299.

[24]   H. Zhang, W. Zhou, Y. Yang, C. Cheng, *Small,* **2017**, 13, 1603840–1603847.

[25]   B. Zhang, L. Wang, Y. Zhang, Y. Ding, Y. Bi, *Angew. Chem. Int. Ed.,* **2018**, 57, 2248–2252.

[26]   K. McDonald, K.-S. Choi, *Energy Environ. Sci.,* **2012**, 5, 8553–8557.

[27]   T. Kim, Y. Ping, G. Galli, K.-S. Choi, *Nat. Commun.,* **2015**, 6, 8769–8778.

[28]   Y. Qiu, W. Liu, W. Chen, W. Chen, G. Zhou, P. C. Hsu, R. Zhang, Z. Liang, S. Fan, Y. Zhang, Y. Cui, *Sci. Adv.*, **2016**; 2, e1501764–e1501764

[29]   B. Zhang, X. Huang, H. Hu, L. Chou, Y. Bi, *J. Mater. Chem. A,* **2019**, 7, 4415–4419.

[30]   W. Wang, J. Dong, X. Ye, Y. Li, Y. Ma, L. Qi, *Small,* **2016**, 12, 1469–1478.

[31]   W. Wang, L. Qi, *Adv. Funct. Mater.,* **2019**, 29, 1807275–1807303.

[32]   X. Chen, J. Ye, S. Ouyang, T. Kako, Z. Li, Z. Zou, *ACS Nano,* **2011**, 5, 4310–4318.

[33]   S. Berglund, A. Rettie, S. Hoang, C. Mullins, *Phys. Chem. Chem. Phys.,* **2012**, 14, 7065–7075.

[34]   X. Zhang, X. Wang, X. Yi, L. Liu, J. Ye, D. Wang, *ACS Appl. Energy Mater.,* **2020**, 3, 3569–3576.

[35]   K. Yuan, Q. Cao, X. Li, H.-Y. Chen, Y. Deng, Y.-Y. Wang, W. Luo, H.-L. Lu, D. Zhang, *Nano Energy,* **2017**, 41, 543–551.

[36]   X. Qiao, Y. Xu, K. Yang, J. Ma, C. Li, H. Wang, L. Jia, *Chem. Eng. J.,* **2020**, 395, 125144–125151.

[37]   W. Zhang, J. Ma, L. Xiong, H.-Y. Jiang, J. Tang, *ACS Appl. Energy Mater.,* **2020**, 3, 5927–5936.

[38]   H. Tan, F. Abdi, Y. Ng, *Chem. Soc. Rev.,* **2019**, 48, 1255–1271.

[39]   S. Kalanur, I.-H. Yoo, J. Park, H. Seo, *J. Mater. Chem. A,* **2017**, 5, 1455–1461.

[40]   B. Jin, E. Jung, M. Ma, S. Kim, K. Zhang, J. Kim, Y. Son, J. Park, *J. Mater. Chem. A,* **2018**, 6, 2585–2592.

[41]   L. Cai, J. Zhao, H. Li, J. Park, I. S. Cho, H. S. Han, X. Zheng, *ACS Energy Lett.*, **2016**, 1, 624−632

B. Jin, E. Jung, M. Ma, S. Kim, K. Zhang, J. Kim, Y. Son, J. Park, *J. Mater. Chem. A,* **2018**, 6, 2585–2592.

[42]   W. D. Chemelewski, J. R. Rosenstock, C. B. Mullins, *J. Mater. Chem. A,* **2014**, 2, 14957−14962.

[43]   S. Wang, T. He, J.-H. Yun, Y. Hu, M. Xiao, A. Du, L. Wang, *Adv. Funct. Mater.,* **2018**, 28, 1802685–1802694.

[44]   M. Shaddad, P. Arunachalam, J. Labis, M. Hezam, A. Al-Mayouf, *Appl. Catal. B Environ.,* **2019**, 244, 863–870.

[45]   S. Zhou, K. Chen, J. Huang, L. Wang, M. Zhang, B. Bai, H. Liu, Q. Wang, *Appl. Catal. B Environ.,* **2020**, 266, 118513–118522.

Graphical abstract

Conformal BiVO$_4$/WO$_3$ nanobowl array photoanode for efficient photoelectrochemical water splitting

Wen Zhang, Meng Tian, Haimiao Jiao, Hai-Ying Jiang* and Junwang Tang*

Northwest University; University College London,
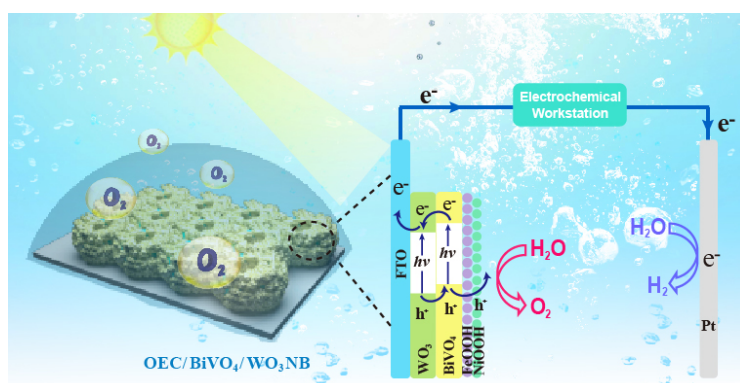
Together with the BiVO$_4$/WO$_3$ NB heterojunction and the deposition of NiOOH/FeOOH cocatalysts, the optimal OEC/BiVO$_4$/WO$_3$NB photoanode shows a markable improvement in photocurrent (~3.05 mA cm^{-2}) and nearly 100% faradaic efficiency for H$_2$ and O$_2$ production.